catalysts

MDPI

Article

Self-Assembled Hybrid ZnO Nanostructures as Supports for Copper-Based Catalysts in the Hydrogenolysis of Glycerol

Lama Omar, Noémie Perret and Stephane Daniele *,†

Institute of Researches on Catalysis and Environment in Lyon, Université Claude Bernard Lyon, Avenue Albert Einstein, 69626 Villeurbanne, France; lama.omar72@gmail.com (L.O.); noemie.perret@ircelyon.univ-lyon1.fr (N.P.)

* Correspondence: stephane.daniele@univ-lyon1.fr

† Present Address: École Supérieure de Chimie Physique Electronique de Lyon, Université Claude Bernard Lyon 1, 43 Bld du 11 Novembre 1918, 69616 Villeurbanne, France.

Abstract: This study describes the use of new ZnO/PAAH hybrid nanomaterials (PAAH = polyacrylic acid) as copper catalyst supports for the hydrogenolysis of glycerol. A study of the synthesis parameters (washing process, temperatures of synthesis and calcination) of these hybrid supports has allowed us to vary their morphology and specific surface area and ultimately the sizes and dispersion of the copper nanoparticles, and to perform a general analysis of their effects on the catalytic performance of the materials. All catalysts were synthesized by the urea deposition-precipitation method (DPU) and were fully characterized to establish a structure–activity relationship. Optimization of the synthesis and catalytic conditions allowed remarkable yields/conversions of the order of 70% for selectivities in 1,2 propanediol of 90%.

Keywords: glycerol hydrogenolysis; ZnO; Cu-based catalyst; hybrid support

Citation: Omar, L.; Perret, N.; Daniele, S. Self-Assembled Hybrid ZnO Nanostructures as Supports for Copper-Based Catalysts in the Hydrogenolysis of Glycerol. *Catalysts* **2021**, *11*, 516. https://doi.org/10.3390/catal11040516

Academic Editor: Francesco Ruffo

Received: 17 March 2021
Accepted: 15 April 2021
Published: 20 April 2021

1. Introduction

Glycerol is largely produced during the transesterification of vegetable oils in the case of biofuel production (10 molecules of glycerol for 1 molecule of biodiesel) with a production expected to reach 41 million m^3 in 2022 [1]. Its valorization is part of one of the strategies to make biodiesel production economically profitable. Although glycerol is a very versatile chemical substance with more than 1000 uses and applications in food products, cosmetics, toiletries and medicines, [2] it can also be transformed into higher value-added products such as ethylene or propylene glycols (1,2-propanediol and 1,3-propanediol) by catalytic hydrogenolysis [3]. For instance, 1,2-propanediol is used in water-based acrylic architectural paints to extend drying time due to its slower evaporation rate compared to water [4] and as a humectant, solvent and preservative in food and for tobacco products. It is used in a variety of consumer products such as coffee beverages, liquid sweeteners, ice cream, whipped dairy products and soft drinks, and as a solvent in many pharmaceutical products, including oral, injectable and topical preparations, such as diazepam and lorazepam, which are insoluble in water [5].

The selectivity in hydrogenolysis reactions, which is accompanied by C–C and C–O bond cleavage, remains a major challenge when, as in the glycerol molecule, several C–C and C–O bonds exist. In the literature, the hydrogenolysis reaction has been carried out using water as a solvent, in a batch reactor under hydrogen pressure and with the addition of different metal catalysts. Catalysts based on Rh [6], Ru [7] and Pt [8] have shown high conversion and variable selectivity towards 1,2-propanediol (1,2-PDO) and 1,3-propanediol (1,3-PDO). Noble metal-free systems, such as those based on Cu, have also recently been investigated as they have the advantages of limiting the cleavage of C–C bonds in favor of C–O bonds [9,10] and are economically viable. The support of a catalyst is also of high importance and, in the case of the hydrogenolysis of glycerol, ZnO has been widely used because of its appropriate acid-base properties.

The use of a copper–zinc catalyst for glycerol hydrogenolysis was first reported in 2004 by Chaminand et al. [11], however, the activity of the catalyst was low with respect to the high catalyst loading and the long reaction time (selectivity to 1,2-PDO of 100% at 19% of conversion under 80 bar of pressure and 180 °C after 90 h). The catalyst preparation method and composition appeared to have a significant role and effect on the performances [12–19]. Most of the work has shown that a 1:1 Cu/Zn molar ratio combined with co-precipitation syntheses often gave the best results in terms of production of 1,2-PDO. Different co-precipitation reagents have been studied such as NaOH or oxalate (via gel), the latter being more efficient as it provided smaller copper particle sizes (6 vs. 12 nm) and therefore a better dispersion (17 vs. 9%) [14]. It was also shown that for this reaction in the presence of water the deactivation of the Cu-ZnO catalyst was mainly due to a loss of specific surface area and the aggregation of the ZnO and Cu nanoparticles [20–22].

High Cu dispersions can be achieved by using supports with high specific surface area. The search for high specific surface area supports with particular morphologies is then a subject of work in full bloom in order to improve or understand catalytic performances. We have recently patented the development of spherical hybrid ZnO/PAAH meso-spheres (PAAH = poly acrylic acid) resulting from the 3D self-assembly of ZnO nanoparticles [23]. These new objects have been extensively studied mainly for their luminescence properties and their application as nanophosphors in light-emitting diode (LED) devices [24,25]. However, since these nanohybrids can reach high specific surface areas (>70 $m^2 \cdot g^{-1}$) compared to conventional ZnO, they are also of interest for catalysis as a support. Here, we report the influence of different synthesis parameters of these objects (washing step, synthesis and calcination temperature) on their specific surface and finally their use as a copper-based catalyst support for the hydrogenolysis of glycerol.

2. Results and Discussion

2.1. Supports Characterizations

In catalysis, the nature of the support plays a major role on the properties of the resulting catalyst. Beyond its acid-base or redox properties, one of its primary functions is to ensure the greatest possible dispersion of the catalyst, hence the frequent search for a support with a high specific surface area. This can be related either to a decrease in size or to a modification of the morphology of the support.

2.1.1. Effect of the Washing Process after Hydrolysis

In the case of ZnO/PAAX systems (PAA2 and PAA5), we decided to optimize firstly the washing step, in terms of specific surface area, on samples prepared at 20 °C in order to be able to discriminate in a relevant way the other synthesis parameters such as temperature of synthesis or calcination. Washing steps are known to be an important step in the synthesis of hybrid nanoparticles as they can affect the specific surface area by removing organic matter that would not be effectively grafted onto the surface. After centrifugation, wet samples of ZnO/PAAX of about 2 g were washed with a specific volume of solvent (from 30 to 90 mL) for 30 min under stirring. For all samples (unwashed and washed), a centrifugation step and oven drying at 80 °C in ambient air were performed to obtain the final powder.

The ZnO/PAA2 samples obtained without washing or after washing with different volumes of ethanol (30 mL, 60 mL, 90 mL) or a 1:1 mixture ethanol/water (60 mL) showed very similar X-Ray Diffraction Analysis (XRD) diffractograms (Figure S1) and Thermal Gravimetric Analysis (TGA) curves (Figure S2). The XRD patterns present the peaks associated with ZnO of hexagonal phase (zincite, PDF 01-083-6338). In addition to the poorly crystalline zincite, a peak at 33° can be observed, attributed to the $Zn(OH)_2$ phase with (211) reflections as in the reference [26]. TG analyses (Figure S2) demonstrated that polyacrylic acid was present in all the samples. The weight loss above 200 °C (Table 1) confirmed that all the polymer was integrated into the hybrid system. The washing step did not impact either the crystallinity of the sample, the ZnO crystallite size (ca. 20 nm), or the

removal of organic matter (ca. 50%). Nevertheless, the Brunauer-Emmett- Teller (BET) and Transmission Electron Microscopy (TEM) results show that the samples were structurally different. Indeed, the BET results (Table 1) show that washing with ethanol significantly increased the specific surface area (S.S.A.) of ZnO/PAA2 samples from 20 to 91 $m^2 \cdot g^{-1}$, especially when the volume of ethanol was large. TEM images (Figure 1) showed the presence of 2D structures and self-assembled spherical aggregates of ZnO nanoparticles in the size range of 150–200 nm. However, ethanol washing induced the "appearance" of a larger quantity of 2D structures composed of zinc and polymer according to Energy Dispersive X-Ray Analysis (EDX), providing a possible explanation for the large increase in specific surface area.

Table 1. Effect of EtOH volume on ZnO/PAA2 nanoparticles' (NPs) properties.

Solvent Volume (mL)	S.S.A./BET ($m^2 \cdot g^{-1}$)	ZnO Crystallite Size/XRD (nm)	TG/Weight Loss [200–600 °C] (%)
unwashed	20	19	40
30 EtOH	60	18	50
60 EtOH	68	22	52
90 EtOH	91	20	50
60 EtOH/H_2O (1:1)	41	16	51

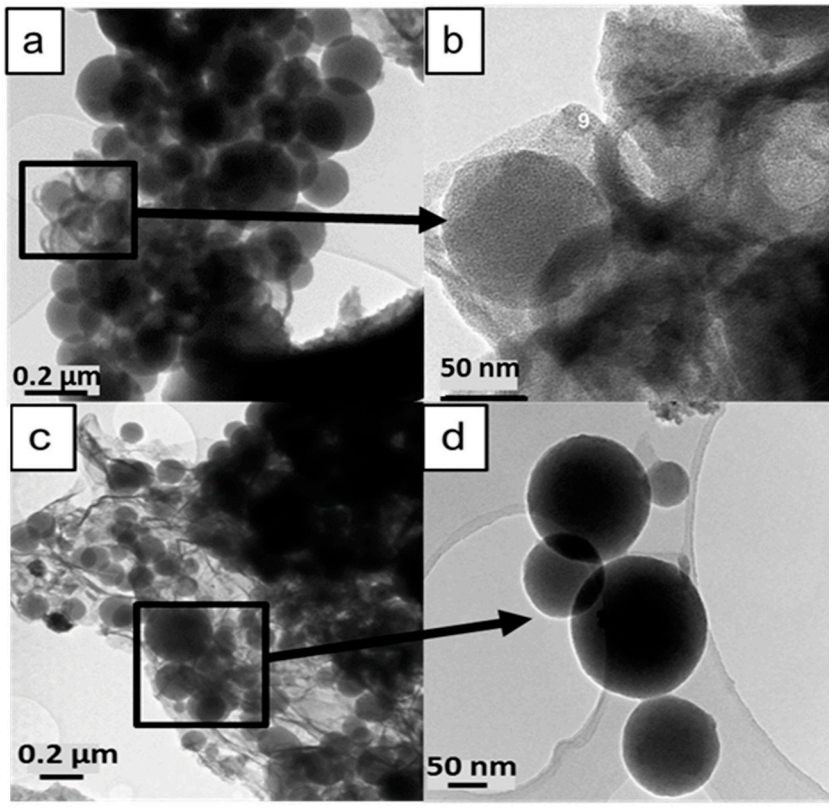

Figure 1. Transmission electron microscopy (TEM) images of ZnO/PAA2 (**a**,**b**) unwashed and (**c**,**d**) washed with 90 mL of EtOH.

If we combine all these data, we can consider that ethanol only removed water whose presence would result in folding these 2D structures onto themselves via hydrogen interactions, for example. The elimination of water would, therefore, make it possible to unfold these structures which would be at the origin of the increase in the specific surface area observed after washing. The presence of water when washing with a water/ethanol mixture (1:1) confirmed this effect with a lower specific surface area of 41 $m^2 \cdot g^{-1}$.

The effect of ethanol washing was extended to ZnO/PAA5. The XRD diffractograms showed that all ZnO/PAA5 samples washed with different volumes of EtOH exhibited an amorphous ZnO structure (Figure S3). Similarly, the TGA analyses also displayed an average loss of 50% for all samples (Figure S4, Table 2). As for ZnO/PAA2 samples, there was an increase in specific surface area from 23 to 75 $m^2 \cdot g^{-1}$ with the increase in the volume of EtOH (Table 2).

Table 2. Effect of EtOH volume on the properties of ZnO/PAA5 NPs.

Solvent Volume (mL)	S.S.A./BET ($m^2 \cdot g^{-1}$)	TG/Weight Loss [200–600 °C] (%)
Unwashed	23	41
30 EtOH	53	42
60 EtOH	58	42
90 EtOH	75	44

In conclusion, as both materials ZnO/PAA2 and ZnO/PAA5 exhibited a larger specific surface area when washed with EtOH, all following materials were washed with 90 mL of EtOH when synthesizing 2 g of ZnO/PAAX.

2.1.2. Effect of the Synthesis Temperature

The XRD results associated with ZnO/PAA2 synthesized at 0 °C, 10 °C and 40 °C showed no difference in crystallinity and crystallite size (Figure 2, Table 3). However BET specific surface area measurements exhibited differences between materials (Table 3), with the highest surfaces (90 $m^2 \cdot g^{-1}$) being obtained at low temperature (0–10 °C). The TG analyses did not show any effect of the synthesis temperature on the inorganic/organic ratios since they were identical (Figure S5, Table 3).

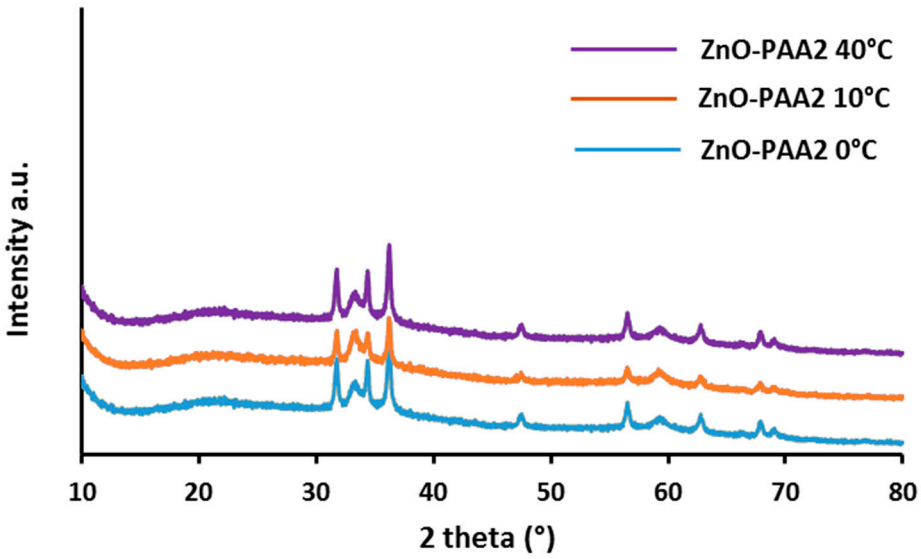

Figure 2. X-ray diffraction (XRD) patterns for ZnO/PAA2 synthesized at different temperatures.

Table 3. Effect of the synthesis temperature on ZnO/PAA2 properties.

Synthesis T (°C)	S.S.A./BET ($m^2 \cdot g^{-1}$)	ZnO Crystallite Size/XRD (nm)	TG/Weight Loss [200–600 °C] (%)	Aggregate Size/TEM (nm)
0	89	23	40	100–200
10	91	25	40	50–200
40	37	24	40	250–350

By comparing TEM images obtained for samples synthesized at 0 °C (Figure 3a) and 40 °C (Figure 3b), the decrease in specific surface area could result from the lower amount of 2D nano-structures and the fusion of some mesospheres into larger aggregates. At low temperatures, it was also possible to find hollow mesospheres, but in very limited numbers.

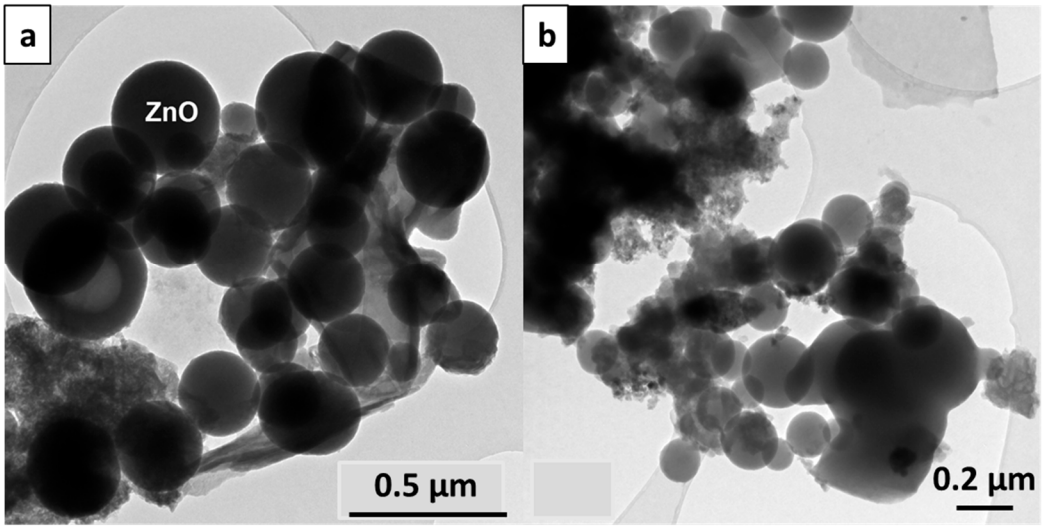

Figure 3. TEM images of ZnO/PAA2 synthesized at (**a**) 0 °C and (**b**) 40 °C.

For ZnO/PAA5, based on XRD measurements, the structure of ZnO crystallites was strongly influenced by the synthesis temperature (Figure 4). At low temperatures, ZnO/PAA5 nanoparticles were mainly amorphous or very small, while an increase in temperature led to an increase in the degree of crystallinity or size of crystallites. The synthesis temperature of 60 °C was added to the three previously selected values to visualize the evolution in terms of structure over a larger temperature range. Table 4 summarizes the different physico-chemical characteristics of the four samples and shows that the specific surface area tends to increase with the synthesis temperature with a maximum of 120 $m^2 \cdot g^{-1}$ at 40 °C, which was the opposite for PAA2. The latter surface area was the highest value obtained in this study. The average crystallite sizes of ZnO around 20 nm and the percentages of organic around 50% (Table 4, Figure S6), were close to those obtained for PAA2.

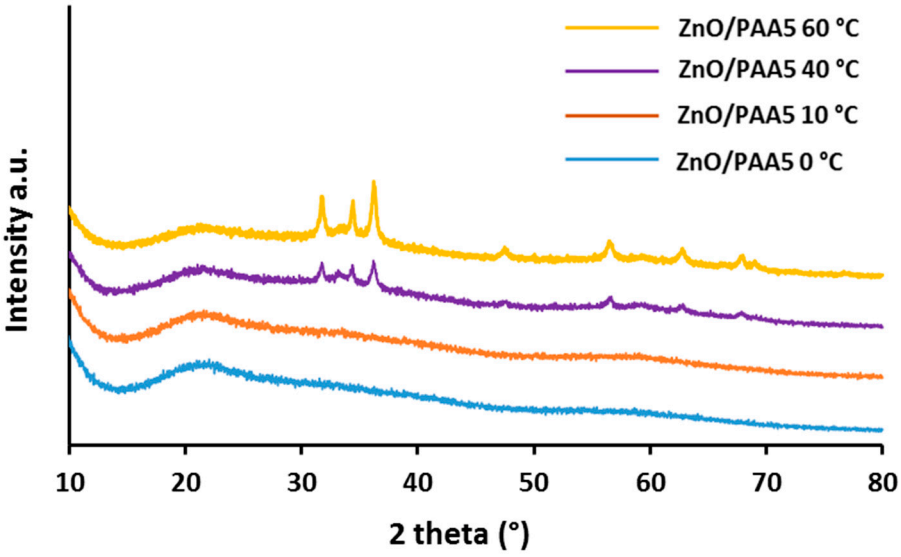

Figure 4. XRD diffraction patterns of ZnO/PAA5 at different synthesis temperatures.

Table 4. Effect of the synthesis temperature on ZnO/PAA5 properties.

Synthesis T (°C)	S.S.A./BET ($m^2 \cdot g^{-1}$)	ZnO Crystallite Size XRD (nm)	Aggregate Sizes/TEM (nm)	TG/Weight Loss [200–600 °C] (%)
0	73	Amorphous	60	41
10	70	Amorphous	–	41
40	120	21	40	38
60	89	18	–	37

TEM and SEM analyses (Figure 5) of the samples synthesized at 0 °C and 40 °C showed that this increase in specific surface area was once again accompanied by the appearance of a 2D phase, a phenomenon already observed for ZnO/PAA2. TEM images showed that at 0 °C, the material was essentially composed of spherical aggregates of an average size of 60 nm associated with a very interesting monodispersity (Figure 5a). This observation was confirmed by the SEM images obtained on this same material where the monodispersity was visualized on a larger scale (Figure 5c). At 40 °C, there was a majority of spherical aggregates on average smaller (40 nm) but also more polydispersed (Figure 5b). The increase in specific surface area could be due to this smaller size or to the presence of 2D nano-structures. SEM images of the material obtained at 40 °C showed that there was an intimate mixture between spherical aggregates and 2D sheets (Figure 5d).

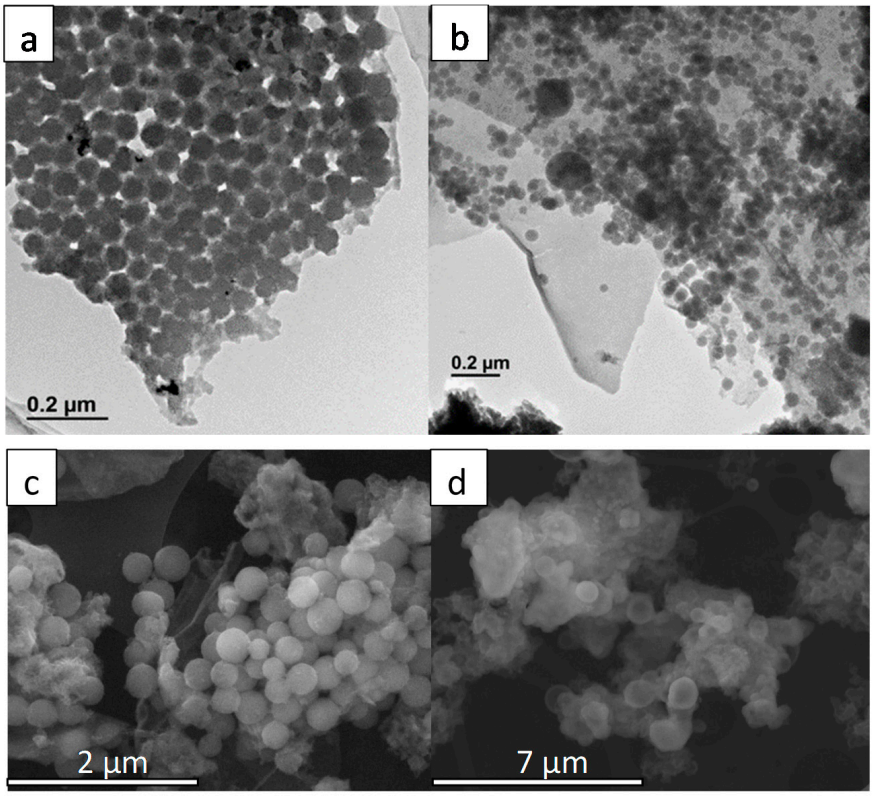

Figure 5. (**a**,**b**) TEM and (**c**,**d**) scanning electron microscopy (SEM) images of ZnO/PAA5 synthetized at 0 °C (**a**,**c**) and 40 °C (**b**,**d**).

Overall, temperature of synthesis did not affect the thermodynamics of both systems since the same raw materials were formed, but it affected the material's morphological evolution through the duration of the synthesis.

2.1.3. Effect of the Calcination Temperature

As shown in the TG analyses in Figures S5 and S6, regardless of their temperature of synthesis, ZnO/PAA2 and ZnO/PAA5 began to degrade thermally at around 300 °C.

The thermal behaviors under air of ZnO/PAA2 and ZnO/PAA5 materials were studied between 300 and 400 °C since they will be calcined at 400 °C after copper deposition.

For ZnO/PAA2 samples, the XRD diffractograms associated with the samples calcinated at 300, 325, 350 and 400 °C (Figure 6) showed an increase in crystallinity with increasing temperature (Table 5). Indeed, at 300 °C, ZnO/PAA2 was 90% amorphous and the 10% of the crystallized phase corresponded to hexagonal ZnO with a crystallite size between 9 nm (calculated with peaks at 47°, 57° and 63°) and 15 nm (calculated with peaks at 31.5°, 34° and 36°). The increase in calcination temperature to 325 °C resulted in an increase in crystallinity to 90% with small crystallites of an average size of 4.4 nm. For temperatures above 325 °C, ZnO/PAA2 was fully crystallized and the average crystallite size increased with the temperature up to 19 nm at 400 °C. The increase in the size and degree of crystallinity of the crystallites with the increase in the calcination temperature can be related to the progressive loss of the organic component. Therefore, it seemed that 350 °C was a transition temperature for the ZnO/PAA2 system. This was confirmed by the TG analyses since the organic content became very low from 350 °C (Table 5).

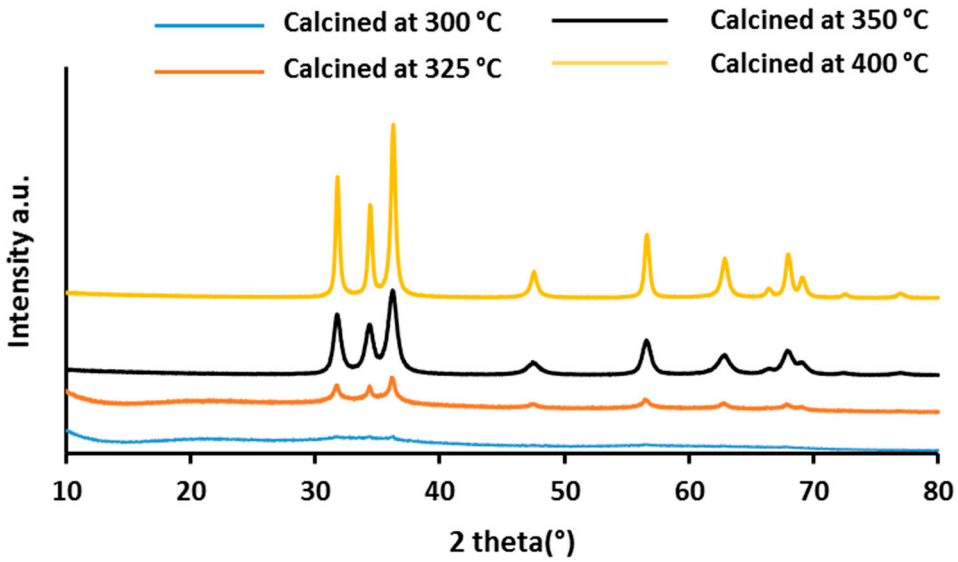

Figure 6. XRD diffraction patterns of ZnO/PAA2 calcined at different temperatures.

Table 5. Properties of ZnO/PAA2 calcined at different temperature.

Calcination Temperature (°C)	S.S.A./BET ($m^2 \cdot g^{-1}$)	ZnO Crystallite Size/XRD (nm)	ZnO Crystallinity (%)	Aggregate Size (TEM nm)	TG/Weight loss [200–600 °C] (%)
300	28	Amorphous	10	120–220	40
325	38	4.4	90	150–200	45
350	51	12.0	100	10–20	5
400	18	19.0	100	20–40	2

Indeed, the TGA curves (Figure S7) confirmed that a large part of the polymer is still present after calcination at 300 °C and 325 °C (Table 5). After calcination at a temperature above 350 °C, ZnO/PAA2 had almost completely lost its organic component (weight loss < 10%). Another change occurred at high calcination temperature, the onset of degradation temperature shifts to a lower value (250 °C instead of 350 °C) indicating a change in the interaction between ZnO and remaining organics.

TEM images associated with samples calcined at different temperatures are shown in Figure 7. ZnO/PAA2 calcined at 300 °C and 325 °C showed the conservation of 3D mesospheric nanoparticle assemblies as for ZnO/PAA2. Heating to a temperature above 325 °C resulted in the total destruction of this morphology (although some spherical

aggregates could still be observed in Figure 7c) which was associated with the increase in crystallite size. This observation showed the need to have the polymer inside the aggregate matrix to maintain the self-assembled morphology.

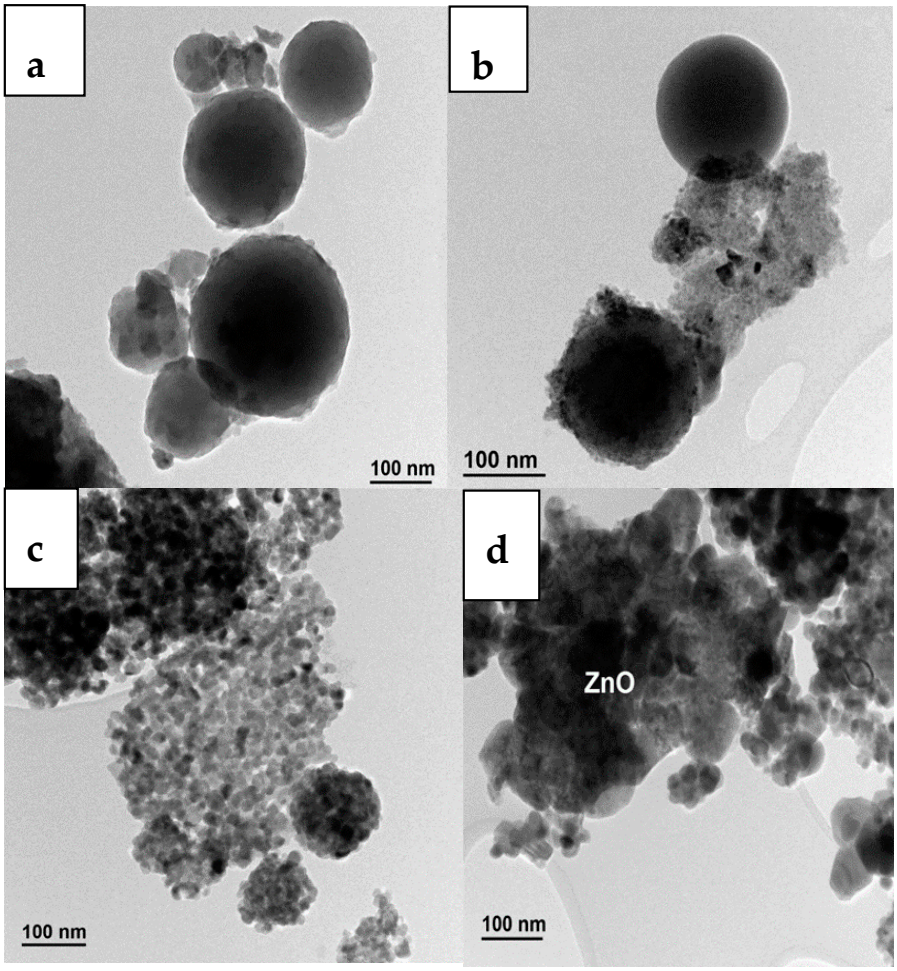

Figure 7. TEM images of ZnO/PAA2 calcined at: (**a**) 300 °C, (**b**) 325 °C, (**c**) 350 °C and (**d**) 400 °C.

Compared to the as-prepared ZnO/PAA2 sample, the BET surface area increased with the increase in calcination temperature, from 20 $m^2 \cdot g^{-1}$ to 51 $m^2 \cdot g^{-1}$ after calcination at 350 °C. At 400 °C, the specific surface area decreased drastically, indicating that ZnO nanoparticles started sintering, in agreement with the TEM images.

For the material ZnO/PAA5 (Table 6), changes in morphology could already be observed after calcination at 300 °C. The XRD diffractograms of the powders calcined at 300, 350 and 400 °C (Figure 8) showed a well-crystallized zincite-type ZnO phase with an average crystallite size of 20 nm for the three samples. TEM images (Figure 9) have shown that 3D hybrid self-assemblies were destroyed at 300 °C to give overall ZnO nanoparticles of hexagonal shapes with an average size between 20 and 30 nm in accordance with XRD results.

Table 6. Properties of ZnO/PAA5 calcined at different temperature.

Calcination T° (°C)	S.S.A./BET ($m^2 \cdot g^{-1}$)	ZnO Crystallite Size/XRD (nm)	ZnO Particle Size/TEM (nm)	TG/Weight Loss [200–600 °C] (%)
300	26	20	20–30	6
350	31	18	20–30	5
400	20	24	20–30	2

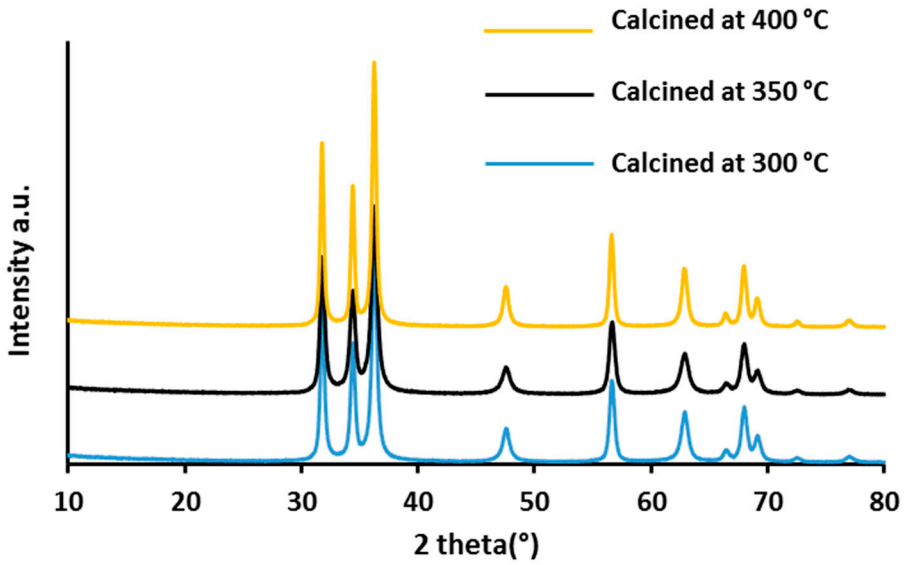

Figure 8. XRD diffraction patterns of ZnO/PAA5 calcined at different temperature.

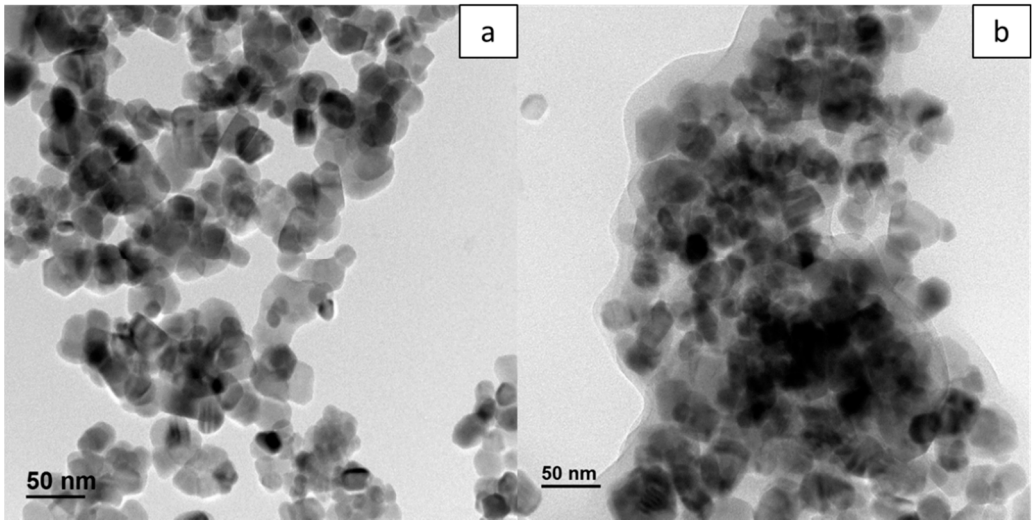

Figure 9. TEM images of ZnO/PAA5 calcined at: (**a**) 300 °C and (**b**) 400 °C.

The TGA curves of solids calcined at 300, 350 and 400 °C showed a weight loss, between 200 and 600 °C, of less than 10%, confirming the almost total degradation of the polymer at 300 °C and a slight evolution of the overall composition (organic/inorganic) of the materials obtained at these three temperatures (Figure S8). As for ZnO/PAA2, the onset of weight loss temperature was lowered by 100 °C, proving that the organic component was of a different nature from the original PAA5.

Compared to ZnO/PAA2, the structure of the ZnO/PAA5 hybrid material has appeared less robust. This observation could be correlated to the smaller size of the aggregates for PAA5 and, therefore, to a larger area of exposure to thermal degradation.

In conclusion, it was demonstrated that the development of reproducible batches of ZnO-PAAX hybrid nanomaterials with well-defined properties (mesosphere and large specific surface area for instance) involved the fine control of many parameters such as synthesis temperature, and washing set-up. The hybrid support exhibited high specific surface area, up to 120 $m^2 \cdot g^{-1}$, which decreased to 20–30 $m^2 \cdot g^{-1}$ after calcination at 400 °C. We were then interested in the effect of hybrid supports, with a wide range of specific surface area, on the properties and catalytic performance of Cu/ZnO catalyst.

2.2. Catalysis Studies

2.2.1. Hydrogenolysis of Glycerol over Cu Supported on Commercial ZnO

The first set of catalysts was developed using a commercial ZnO. The XRD pattern of this material (Figure S9a) shows that it was very well crystallized (size of 50 nm) with the hexagonal phase of zincite. On the other hand, TEM images (Figure S9b) showed large particles ranging from 50 to 200 nm with heterogeneous shapes. The high particle size was reflected in the specific surface area which was very low (13 $m^2 \cdot g^{-1}$).

Different weight percentages of copper (from 2.5 to 20 %wt) were deposited by deposition-precipitation method with urea (DPU) on the support. After synthesis, the dry powder was calcined at 400 °C in air, then reduced at 300 °C under H_2, and finally passivated. The XRD patterns shown in Figure S10 correspond to the different stages of the synthesis of 5% Cu/ZnO_{20} (5 %wt of Cu; synthesized with a solution of Cu^{2+} at 20.8 mM), as representative examples. The hexagonal phase of ZnO was always present with an average crystallite size of 60 nm. After DPU, a new peak appears at 28° corresponding to the monoclinic phase $Cu_2(NO_3)(OH)_3$ (PDF 00-045-094). Urea played a role of a delay base by decomposing into ammonium and cyanate when increasing the temperature, which led to an increase of the pH (up to 8). Hence, Cu^{2+} ions precipitated with the nitrates ions in the form of $Cu_2(NO_3)(OH)_3$ onto the surface of ZnO, as previously reported by Louis et al. over TiO_2 [27]. We cannot exclude the formation of $(Cu,Zn)(CO_3)(OH)_2$ (PDF number 00-036-1475) which overlaid with $Cu_2(NO_3)(OH)_3$. This phase would result from a partial dissolution of ZnO in basic media followed by co-precipitation. After calcination, the later phase transformed into monoclinic CuO (PDF number 00-045-0937) where the main peak was at 38°. Hydrogen then reduced CuO to cubic Cu^0 (PDF number 04-013-9963) with the main peaks at 43°, 51° and 74°. It is worth noting that the Inductively Coupled Plasma (ICP) results are consistent with the theoretical weight percentage proving the total deposition of copper onto the commercial support (Table 7).

Table 7. Cu supported on commercial ZnO: characterization and catalytic properties.

Entry	Catalysts [a]	$[Cu^{2+}]$ (mM) [b]	Cu [c] (%wt)	Cu^0 Size(nm) [d]		Conversion [e] (%)	Selectivity (%) [e]	
				B.R.	A.R.		1,2 PDO	EG
1	$2.5\%Cu/ZnO_{20}$	20.8	2.3	13	20	2	99	1
2	$5\%Cu/ZnO_{20}$	20.8	4.9	13	21	10	92	8
3	$10\%Cu/ZnO_{20}$	20.8	9.7	15	20	25	90	10
4	$15\%Cu/ZnO_{20}$	20.8	15.5	14	45	22	91	9
5	$20\%Cu/ZnO_{20}$	20.8	19.2	20	35	15	91	9
6	$10\%Cu/ZnO_5$	5.2	11.1	23	x	19	97	2
7	$10\%Cu/ZnO_{10}$	10.4	10.3	20	x	20	95	4
8	$10\%Cu/ZnO_{40}$	40.8	10.3	15	x	22	94	5
9	$10\%Cu/ZnO_{80}$	81.6	9.3	11	40	16	98	1

[a] The first number refer to the Cu loading; the subscript refer to $[Cu^{2+}]$ concentration. [b] concentration of Cu^{2+} in the solution at the beginning of the synthesis. [c] actual loading, determined by inductively coupled plasma (ICP) analysis. [d] B.R = Before reaction. A.R. = After reaction. [e] After 24 h.

A series of catalysts (entry 1–5; Table 7) was synthesized using the same concentration of precursor during the synthesis ($[Cu^{2+}]$ = 20.8 mM) and different copper final loading (2.5; 5; 10; 15; 20 %wt). For copper contents below 15 %wt, the size of Cu^0 crystallites before catalysis was constant (ca. 14 nm). On the other hand, for $20\%Cu/ZnO_{20}$, the size of Cu^0 crystallites increased to 20 nm. The increase in crystallite size with copper charges has been reported in several studies using different preparation methods. Karelovic et al. have prepared Cu/ZnO by wet impregnation and obtained Cu^0 crystallites of 25 and 35 nm, at 3 and 15 %wt of Cu, respectively [28].

Another set of catalysts (10%Cu/ZnO) were synthesized using different concentration of copper solutions at the beginning of the synthesis (entries 6–9, Table 7). At the same weight percentage, the crystallite main size showed a decrease when the Cu^{2+} concentration was increased. To our knowledge, there is no study showing the effect of precursor

concentration at the same weight percentage for the synthesis of Cu catalysts by DPU. At higher concentration and lower volume, the kinetic was different and the precursor must precipitate more rapidly. However, the temperature and pH increased with time; therefore, at higher concentration, the precipitation might occur at lower temperature and/or lower pH. This might result in the formation of a larger number of nuclei and/or a better support/precursor interaction, which would result on the formation of smaller particles.

After characterizing the main properties of these catalysts, the conversion of glycerol into 1,2-propanediol (1,2-PDO) was studied in a batch reactor at 200 °C, under 30 bar of H_2. When using Cu/ZnO in water, the reaction follows the dehydration hydrogenation route as shown in Scheme 1. As a first step, the dehydration takes place on the surface of ZnO due to its acidic properties resulting in acetol as intermediate [8]. It is then transformed over the copper surface into 1,2 propanediol (1,2-PDO) as major product and ethylene glycol (EG) as secondary product. As representative examples, the evolution of the conversion and selectivity to 1,2-PDO versus time, associated with the entries 1–5 (Table 7), are shown in Figure S11. The conversion and selectivity after 24 h obtained with all the catalysts prepared with the commercial ZnO are summarized in Table 7. The Cu/ZnO molar ratios, the amount of 1,2 PDO produced per mol of Cu (in 24 h) and the initial rates (V_0) are included in Table S1. All the catalysts were highly selective (>90%) towards 1,2-PDO and the remaining 10% was mainly EG and traces of ethanol. This was in agreement with the literature where Cu/ZnO is known to exhibit high selectivity towards 1,2-PDO under these reaction conditions [11]. For all the reactions, the carbon balance was always above 95%.

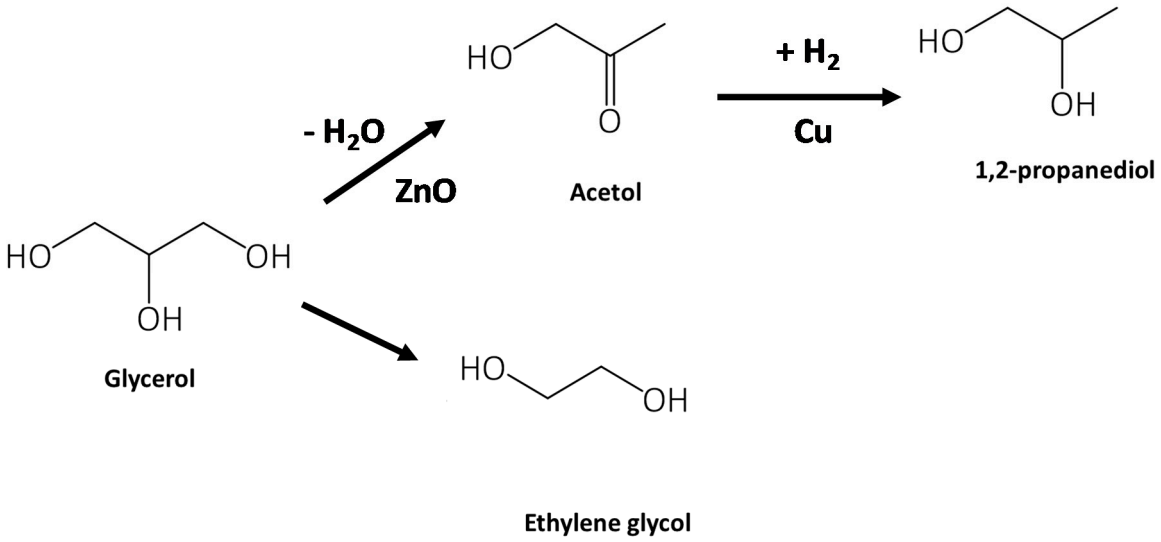

Scheme 1. Reaction pathway associated with glycerol hydrogenolysis over Cu/ZnO catalysts.

At low weight percentage of copper (2.5%wt Cu/ZnO_{20}), the conversion was very low, only 2% of glycerol was converted. As the same mass of catalyst was used for all the reactions (500 mg), an increase in the weight percentage of copper to 10% resulted in an increase in catalyst conversion. At higher weight percentages of copper (15% and 20%), the support began to be highly charged and might have been inaccessible to glycerol molecules. Actually, the surface density of Cu was around 8 atoms/nm^2 for a weight percentage of copper higher than 8 %wt, which correspond to a monolayer [17]. Therefore, the low conversion and low initial rate (V_0) at high loading could come from the saturation of the ZnO, preventing the support from hydrolyzing glycerol to acetol in the first step. There is a clear dependence on the initial rates, and the amount of 1,2-PDO produced per mol of Cu, with the Cu/Zn molar ratio, with an optimal for Cu/Zn = 0.14. This behavior was reported by Gao et al. who demonstrated that increasing the Cu/Zn molar ratio from 0 to 1.86 led to an increase in glycerol conversion from 0 to 48% followed by a decrease to 33% with increasing copper content [29]. Another factor contributing to this

low conversion was the sintering of copper and ZnO particles. Indeed, Figure S12 shows the diffractograms associated with 2.5%Cu/ZnO_{20} and 20%Cu/ZnO_{20} before and after the test. For the catalysts with low Cu loading, the crystallites did not show any strong structural changes. However, for 15%Cu/ZnO_{20} and 20%Cu/ZnO_{20}, the crystallite sizes showed a strong sintering of Cu^0 nanoparticles (Table 7) and ZnO (from ca. 50 to 70 nm). However, the activity of Cu/ZnO in the hydrogenolysis of glycerol is known to depend strongly on Cu and ZnO particle sizes.

The increase in the concentration of the Cu^{2+} solution for 10%Cu/ZnO (Table 7, entries 3, 6–9) resulted in an increase, followed by a decrease in catalyst conversion, with an optimum at 25% for Cu^{2+} concentration of 20.8 mM. The same trend was observed for the initial rates and the amount of 1,2-PDO produced per mol of Cu (Table S1). The lower conversion obtained for 10%Cu/ZnO_{80} could be explained by the sintering of copper particles during the reaction. The size of Cu^0 crystallites increases from 11 to 40 nm for 10%Cu/ZnO_{80} compared to a slight increase from 15 to 20 nm for 10%Cu/ZnO_{20}. The sintering of copper particles during the reaction is a common phenomenon for copper-based catalysts and has been reported by many groups. In the article of Bienholz et al. [14] copper particle size increases from 15 nm before catalysis (CuO/ZnO) to 40 nm after catalysis (Cu/ZnO) for the same catalytic reaction with 46% of conversion after 7 h of reaction. The XRD diffractograms after catalysis presented in Figure S13 showed the appearance of a new phase containing carbon, $(Cu,Zn)_5(CO_3)_2(OH)_6$ (PDF 00-038-0154), for 10%Cu/ZnO_{20}. Ethylene glycol and traces of ethanol were detected by gas chromatography (GC) analysis of this catalyst. Therefore, the incorporation of the carbon must be associated with the C–C cleavage. The phase containing carbon was not observed after reaction for 10%Cu/ZnO_{80} which was less active. To our knowledge, few studies reported characterization of Cu/ZnO catalysts after the reaction. Recently, the group of Biswas [19] published an article showing the change of structure of Cu-Zn/MgO after hydrogenolysis of glycerol but without identifying the additional peaks.

The TEM images of 10%Cu/ZnO_{20} and 10%Cu/ZnO_{80} before the reaction (Figure S14) showed similar particle size and morphology for both catalysts, although it was difficult to distinguish easily copper and ZnO by TEM due to their close atomic number. TEM images of catalysts after reaction, in agreement with XRD data, showed significant differences in morphology in two aspects: 10%Cu/ZnO_{20} exhibited lamellar structures characteristic of layered double hydroxides (LDH) while for 10%Cu/ZnO_{80}, the sintering of copper nanoparticles was clearly visible. The presence of CO_3 and OH on the used 10%Cu/ZnO_{20} was confirmed by TGA where a weight loss of about 11% between 200 and 600 °C was observed, which was not the case for 10%Cu/ZnO_{80}.

2.2.2. Hydrogenolysis of Glycerol over Cu Supported on ZnO/PAAX

The catalysts were prepared with ZnO/PAA2 and ZnO/PAA5 supports, washed with 90 mL EtOH. The supports ZnO/PAAX were synthesized at different temperatures (0; 10; 20; 40 °C) and used as-synthesized (NC, not calcined) or after calcination at 300 °C (C300) or 400 °C (C400). The addition of copper was done by the DPU method ($[Cu^{2+}]$ = 20.8 mM) aiming for varied Cu weight percentage (5; 10; 20; 40 %wt). The effect of these parameters (temperature of synthesis of the support, post-treatment of the support, copper loading) on the catalytic hydrogenolysis of glycerol of Cu/ZnO/PAAX were investigated. Table 8 and Table S2 present some of the properties of the catalysts, as well as the conversion, selectivity and the amount of 1,2-PDO produced per mol of Cu, after 24 h. The specific surface areas of the supports were reported in the previous section. After DPU, calcination and reduction, all the catalysts exhibited the same specific surface area of about 25 $m^2 \cdot g^{-1}$.

When comparing the catalysts based on ZnO/PAA2 support synthesized at 0 °C (Cu/ZnO/$PAA2_{0\text{-}NC}$), the conversion increased from 4% to 70% with the increase of copper loading from 5 to 20 %wt. This was partially attributed to the higher ratio $n_{Cu}/n_{glycerol}$ at higher loading of copper. Cu^0 sizes were around 12 nm for these catalysts (Entries 1–3, Table 8). However, Cu crystallite size increased up to 20 nm when increasing the loading

to 38 %wt (40%Cu/ZnO/PAA2$_{0\text{-NC}}$). This was associated with a decrease in conversion from 70% to 4%. As with the commercial ZnO, the high coverage of copper must block the active sites of ZnO. The second reason for this low conversion must be the deactivation of 40%Cu/ZnO/PAA2$_0$ due to the sintering of copper particles during catalysis as Cu^0 increased from 20 nm to 40 nm. An important result was the possibility of depositing a high copper charge (38 %wt), with relatively small crystallite size (20 nm) on the surface of such supports. This could be beneficial for other catalytic reactions where ZnO has no role in the reaction mechanism. The selectivities towards 1,2-PDO were similar for all the catalysts, independent of the support. It went from 98% towards 1,2-PDO at low conversation (<30%), down to 86–90% at high conversion (Figure S15). Ethylene glycol was formed as the major by-product.

Table 8. Characterization and catalytic results associated with Cu/ZnO/PAAX.

Entry	Catalysts [a]	Cu (%wt) [b]	Cu^0 Size (nm) [c]		Conversion [d] (%)	Selectivity [d] (%)	
			B.R.	A.R.		1,2 PD	EG
1	**5%Cu/ZnO/PAA2$_{0\text{-NC}}$**	**5.5**	**12**	**12**	**4**	98	2
2	10%Cu/ZnO/PAA2$_{0\text{-NC}}$	10.2	13	14	48	90	11
3	**20%Cu/ZnO/PAA2$_{0\text{-NC}}$**	19.3	12	16	**70**	87	12
5	40%Cu/ZnO/PAA2$_{0\text{-NC}}$	37.9	20	40	4	94	6
6	20%Cu/ZnO/PAA2$_{10\text{-NC}}$	20.9	15	18	60	89	11
7	20%Cu/ZnO/PAA2$_{20\text{-NC}}$	21.2	21	25	55	88	12
8	20%Cu/ZnO/PAA2$_{40\text{-NC}}$	21.0	21	26	27	89	11
9	**20%Cu/ZnO/PAA5$_{0\text{-NC}}$**	23.2	18	20	64	**99**	**1**
10	**20%Cu/ZnO/PAA5$_{20\text{-NC}}$**	20.5	17	20	**70**	87	13
11	20%Cu/ZnO/PAA5$_{40\text{-NC}}$	19.9	20	25	56	89	11
12	20%Cu/ZnO/PAA2$_{20\text{-C400}}$	22.1	19	21	55	88	12
13	20%Cu/ZnO/PAA5$_{20\text{-C300}}$	17.0	13	24	27	90	10

[a] The first numbers refer to the Cu loading; the subscript refers to the temperature of synthesis of the support (0, 10, 20, 40 °C) and the post-treatment of the support before deposition-precipitation method with urea (DPU) (NC, not calcined; C300, calcined at 300 °C; C400, calcined at 400 °C). [b] actual loading, determined by ICP analysis. [c] B.R = Before reaction. A.R. = After reaction. [d] after 24 h.

Comparing the catalysts based on ZnO/PAA2 supports synthesized at different temperature (entries 3, 6–8), when the temperature decreased, from 40 to 0 °C, the Cu^0 crystallite size decreased, from 21 to 12 nm, and the conversion increased, from 27% to 70%. This must be related to the higher surface area of the support synthesized at lower temperature (ca. 90 $m^2 \cdot g^{-1}$). These remarkable values in terms of specific surface area for ZnO/based system allowed high dispersions of copper and the achievement of the small Cu^0 sizes (12 nm). Moreover, if we look back to the effect of the synthesis temperature on the NPs of ZnO, the main difference resided in the morphology of the material. It appeared that the presence of 2D sheets at low temperature might generate higher dispersion of Cu particles than the support synthesized at high temperature.

For all the catalysts prepared from the different ZnO/PAA5 supports (entries 9–11, Table 8), the effect of specific surface area was less obvious since the best conversions were obtained with the two supports prepared at 0 and 20 °C which had lower specific surface areas (73–75 $m^2 \cdot g^{-1}$) compared to that prepared at 40 °C (120 $m^2 \cdot g^{-1}$). Nevertheless, these performances were consistent with the slightly larger Cu^0 crystallite size (20 nm) for ZnO/PAA5$_{40\text{-NC}}$, which could be due to a poorer dispersion of copper on the 2D structures strongly present in this sample. The excellent selectivity of 20%Cu/ZnO/PAA5$_{0\text{-NC}}$ in 1,2-PDO (99%, entry 9) whose support had been synthesized at 0 °C must be underlined. Total selectivity at high conversion when using copper based catalysts has been reported in few studies but in presence of organic solvents as in reference [30] where the authors used copper nanoparticles supported on AlO_x in dioxane.

Finally, the calcinations of ZnO/PAA2$_{20}$ and ZnO/PAA5$_{20}$ supports before copper deposition did not bring any benefit on the performance of the final catalysts in terms of conversion and selectivity (Entries 12–13, Table 8).

2.2.3. Structural Stability and Catalytic Recycling of Cu/ZnO/PAAX Catalysts

Figure S16 shows the XRD patterns associated with 20%Cu/ZnO/PAA2$_{0\text{-NC}}$ after reactions. When the reaction was conducted for 24 h, the catalyst exhibited the carbonic phase $(Cu,Zn)_5(CO_3)_2(OH)_6$. However, when the reaction was stopped after 6 h, the catalyst did not show any structural changes, confirming that the new phase was appearing at high conversion (>60%) due to the formation of products resulting from C–C cleavage. Nevertheless, in both cases, the ZnO crystallite sizes increased, hence the hydrothermal stability of the ZnO particles was limited [20,21].

In order to study the stability of 20%Cu/ZnO/PAA2$_{0\text{-NC}}$, a recyclability test was carried out with a higher amount of 1.5 g and the catalyst recycled without pre-treatment (Table 9). Unfortunately, the catalyst was barely active (8%), resulting in a decrease in 1,2-PDO selectivity to 75% and an increase in EG selectivity to 22% with the appearance of many unidentified by-products. In a second step, the catalyst used was calcined at 400 °C and reduced to 350 °C. The conversion increased to 48% and the selectivity towards 1,2-PDO was in line with the first series of tests (90%).

Table 9. Recycling of 20%Cu/ZnO/PAA2$_{0\text{-NC}}$.

Test	ZnO Size (nm)		Cu^0 Size (nm)		Conversion (%)	Selectivity (%)	
	B.R.	A.R.	B.R.	A.R.		1.2 PDO	EG
Reused	35	46	25	26	8	75	22
Retreated and reused	22	35	20	24	48	90	10

XRD diffractograms (Figure S17) showed that the catalyst after the first reaction and after the second reaction (reused) exhibited the same diffractograms, i.e., presence of $(Cu,Zn)_5(CO_3)_2(OH)_6$ phase. The catalyst reused without treatment was not very active, hence $(Cu,Zn)_5(CO_3)_2(OH)_6$ phase might be detrimental to the activity. After calcination and reduction, the retreated catalyst had the same structure as the fresh catalyst. This result meant that Cu/ZnO/PAAX could be regenerated.

Figure 10 shows the catalytic results obtained after 24 h over selected catalysts. The substitution of the commercial ZnO by ZnO/PAA2 (synthesized at 0 °C) led to an increase of the conversion from 25% to 70%. This can be related to the exceptional properties of the hybrid ZnO compared to the commercial one as shown in the upper section. Comparing the properties of the catalysts using commercial ZnO or ZnO/PAAX as support, the two families of catalysts showed similar copper crystallite size which ranged between 11 and 23 nm depending on the copper weight percentage. However, under the same synthesis and catalytic conditions, the conversions were always higher with ZnO/PAAX than ZnO commercial. It is worth noting that most of the literature focused on the hydrogenolysis of glycerol over Cu-ZnO systems reporting a conversion below 50%, with selectivity to 1,2-PDO in the range 77–100%, when working under similar reaction conditions (T = 180–200 °C, P_{H2} = 20–80 bars, batch reactor) [11–14,17,18,20]. There is only one study reporting almost full conversion, when working at 220 °C, 50 bars of H_2, with a semi-continuous system [21]. Our synthesis method using polyacrylic acid allows the formation of Cu-ZnO with some of the best catalytic properties reported in the literature, achieving 70% conversion of glycerol, and over 60% yield of 1,2-PDO.

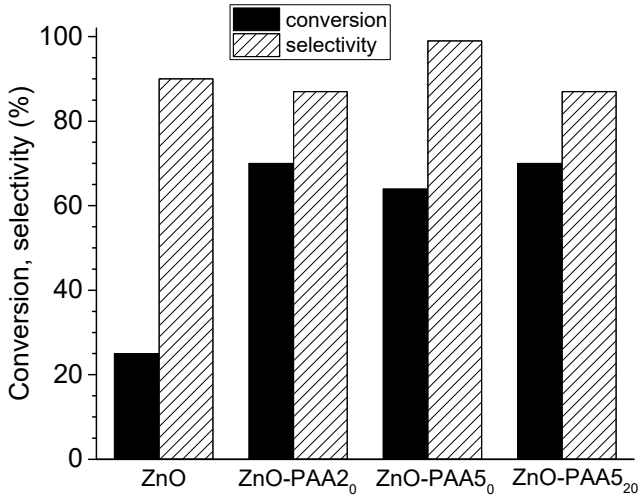

Figure 10. Conversion and selectivity after 24 h, for the hydrogenolysis of glycerol over 10%Cu/ZnO_{20} (ZnO), 20%Cu/ZnO/$PAA2_{0\text{-NC}}$ (ZnO/$PAA2_0$), 20%Cu/ZnO/$PAA5_{0\text{-NC}}$ (ZnO/$PAA5_0$) and 20%Cu/ZnO/$PAA5_{20\text{-NC}}$ (ZnO/$PAA5_{20}$).

3. Experimental Section

3.1. Materials

$ZnEt_2$ (15 %wt in toluene), $Cu(NO_3)_2.3H_2O$ (99.9%), glycerol (99.5%), urea (99%) and aqueous solutions of polyacrylic acid (PAAH, 50 %wt in water) of molecular weight of 2000 (PAA2) and 5000 g·mol^{-1} (PAA5) were purchased from Merck (Darmstadt, Germany) and used as received. Commercial ZnO (99.9%) was supplied from Alfa Aeasar (Haverhill, MA, USA). All the gases (H_2, O_2/N_2, air) were supplied by Air liquide (Paris, France).

3.2. ZnO/PAAX (X = 2 or 5) Synthesis

The ZnO/PAAX (X = 2 or 5) samples were synthesized as described in our previous publications [23–25] (Equation (1)) but optimized for 2 g up-scaling: 2.52 g of polyacrylic acid (1.26 mmol) were dissolved in 200 mL of distilled water to give a concentration of 0.63 %wt of PAAX of molecular weight of 2000 and 5000 g·mol^{-1} designated as PAA2 and PAA5, respectively. Under vigorous stirring, in an inert atmosphere and at room temperature, 14.4 mL of $ZnEt_2$ (16 mmol) were added to the aqueous PAAX solution in a single step. The reaction was exothermic and produced ethane that was eliminated by a bubbler connected to the flask. After one hour, the white suspension was centrifuged at 8000 rpm for 20 min, and washed and dried in the oven under air at 80 °C to give about 2 g of a white powder.

$$Zn(CH_2CH_3)_2 + PAAX + H_2O \rightarrow ZnO/PAAX + 2\ CH_3CH_3 \quad (X = 2 \text{ or } 5) \quad (1)$$

We varied the washing step (volume and composition of the H_2O/ethanol mixture), the synthesis temperature (from 0 to 40 °C), and finally the calcination temperature (up to 400 °C) in order to study their effect on the properties of the resulting Cu/ZnO catalyst.

3.3. Catalysts Preparations

The Cu/ZnO catalysts were prepared by deposition-precipitation method with urea (DPU). In a typical procedure, 7.6 g of $Cu(NO_3)_2{\cdot}3H_2O$ (31 mmol) were dissolved in 200 mL of distilled water to give a 0.157 M concentration of the solution. 1 g of commercial ZnO (12 mmol) or molar equivalent of the hybrid ZnO/PAAH, was added to a 500 mL flask. Different volumes of already prepared copper nitrate solution were added to the ZnO depending on the final weight percentage of Cu. 4 g of urea (66 mmol) were used as precipitating agent and a calculated volume of distilled water was added to obtain a final Cu^{2+} concentration of 20.8 mM. This concentration was optimized through the study of the

commercial ZnO support. The solution was heated to 95 °C with an increase of 1 °C·min^{-1} for 3 h. The resulting precipitates were filtered and washed with 100 mL of distilled water. After drying at 100 °C overnight, the solids were calcined at 400 °C for 4 h in a furnace. They were then reduced in a cell under H_2 at 350 °C at a flow of 50 mL·min^{-1} for 1 h and finally passivated for 30 min under a flow of 1% O_2/N_2 at room temperature.

A series of Cu/ZnO catalysts with nominal Cu loadings of 2.5, 5, 10, 15 and 20 %wt was obtained by using commercial ZnO as reference support to compare with homemade ZnO/PAAH.

3.4. Characterization of Catalysts

Powder X-ray diffraction (XRD) patterns of the samples were recorded using an Advance Diffractometer D8A25 equipped with a nickel filter, a copper tube (λKα (Cu) = 1.54184 Å) and a multi-channel fast detector (LynxEye 192 channels an active length of 2.947°) (Bruker, Billerica, MA, USA). ZnO samples and the Cu/ZnO catalysts were scanned at 0.04° s^{-1} over the range $10 \leq 2\theta \leq 80°$. Phase identification was achieved by using Diffrac.Eva software. The mean crystallite sizes (d_M) were estimated using the Scherrer equation from the half-width of the XRD broadening peak in a diffraction pattern: $d_M = 0.9\lambda/\beta\cos\theta$, in which λ is the X-ray wavelength (λ =1.54184 Å), θ is the Bragg angle, and β is the line broadening at half-maximum of the diffraction peak. For ZnO the peaks used to calculate the crystallite size were at 2θ = 47.5°, 57° and 63° while for reduced copper the main peaks were at 43°, 51° and 74°. The crystallinity was calculated by Rietveld refinement with FullProf software. The elemental analysis of Cu was measured by inductively coupled plasma optical emission spectroscopy (ICP-OES ACTIVA) in IRCELYON (Horiba Jobin Yvon, Longjumeau, France). Before analysis, the solid samples were dissolved in an acid mixture and heated at 250–300 °C. The Brunauer-Emmett- Teller (BET) specific surface area of the samples was determined from the N_2 physisorption at 77 K by using an ASAP 2020 apparatus (Micromeritics, Merignac, France). Before the measurements, the materials were degassed at 150 °C for 2 h under ultra-high vacuum (10^{-4} mbar). The specific surface area was calculated from the obtained isotherms. Scanning electron microscopy (SEM) and transmission electron microscopy (TEM) images were obtained by using an ESEM-FEG FEI XL30 and a JEOL 2010 instruments (JEOL Ltd, Tokyo, Japan) and an Oxford Link Isis EDX (energy-dispersive X-ray spectroscopy) microanalysis system (Oxford Instruments, Abingdon-on-Thames, UK), respectively. Thermogravimetric analysis (TGA) was conducted using few mgs of the powder heated at 5 °C min^{-1} to 700 °C under air, using a TGA/differential scanning calorimetry (DSC) 1 thermal analysis MX1 from, Stare system, gas controller GC200 (Mettler Toledo, Greifensee, Switzerland).

3.5. Catalytic Tests

The glycerol hydrogenolysis was performed using a 300 mL reactor autoclave (Parr 4560, Parr Instrument Company, Moline, IL, USA). Typically, 100 mL of glycerol aqueous solution (2.14 wt%) and 0.5 g of catalyst were loaded into the reactor. After sealing, the autoclave was purged three times with Ar. Then the heating was turned on to reach 200 °C, and the stirring was set 1000 rpm. When the temperature was stable, the reactor was pressurized with H_2 (PH_2 = 30 bar). Liquid samples were collected periodically during the reaction, up to 24 h. The concentration of the products was determined after analyzing the samples by gas chromatography GC-2010 + FID (Shimadzu, Kyoto, Japan) and a column FFAP 30 × 0.25 μm (Phenomenex, Torrance, CA, USA). At the end of the reaction, the autoclave was cooled down, the pressure was released, and the suspension was collected and filtered.

The conversion of glycerol as well as the selectivity and yield of the product i were calculated based on liquid products using Equations (2) and (3):

$$\text{Conversion}(\%) = \frac{C_0^{\text{substrate}} - C_t^{\text{substrate}}}{C_0^{\text{substrate}}} \times 100 \quad (2)$$

with:

- $C_0^{substrate}$: Initial concentration of substrate (in mol·L^{-1});
- $C_t^{substrate}$: Concentration of substrate at time t (in mol·L^{-1}).

$$\text{Selectivity}(\%) = \frac{C_t^{\text{product i}} \times N_C^{\text{product i}}}{\left(C_0^{substrate} - C_t^{substrate}\right) \times N_C^{subsrate}} \times 100 \quad (3)$$

with:

- $C_t^{\text{product i}}$: Concentration of product i at time t (in mol·L^{-1});
- $N_C^{\text{product i}}$: Number of carbon atoms in the product i;
- $N_C^{subsrate}$: Number of carbon atoms in the substrate.

The initial reaction rate was calculated based on the slope of the linear curve,

$$V_0\left(\text{mmol}_{\text{Substrate}}\ \text{mol}_{\text{Cu}}^{-1}\ \text{h}^{-1}\right) = \frac{\text{mmole of reactant}}{\text{mole of Cu} \times \text{time}} \quad (4)$$

4. Conclusions

In conclusion, we demonstrated that syntheses of hybrid ZnO/PAAX (X = 2 or 5) mesospheres with 3D self-assembly were generally accompanied by the presence of 2D structures. These latter, which seemed to be preferred at high temperature for PAA5 and at low temperature for PAA2, led to a significant increase in the specific surface area of the final material. Thus, for ZnO/PAA2, synthesis at 0–10 °C was associated with a high specific surface area of 91 $m^2 \cdot g^{-1}$ while for ZnO/PAA5, a maximum specific surface area of 120 $m^2 \cdot g^{-1}$ was obtained at 40 °C. Ethanol washing is favorable to an increase in the specific surface area by affecting the surface dehydration of aggregates and by decreasing Van der Waals interactions between aggregates (or even 2D sheets) (i.e., hydrogen interactions). We have also shown that the thermal stability of ZnO/PAA2 and ZnO/PAA5 systems depended on the size of the aggregates and, therefore, on the molecular weight of the polymer. ZnO/PAA5, forming smaller aggregates, was less thermally stable with total degradation of the hybrid system from 300 °C while the ZnO/PAA2 mesospheres were still observable at 325 °C.

These high specific surface area ZnO-based supports were compared to commercial ZnO (11 $m^2 \cdot g^{-1}$) for the deposition of copper nanoparticles and catalytic performances. They allowed a non-sintering copper process even with a high Cu loading (35%wt) and achieved remarkable conversions (>60–70%) and high selectivities (>90%) in 1,2-PDO. Further works are in progress to stabilize the catalyst in an aqueous media during the reaction by adding aluminium oxide.

Supplementary Materials: Supplementary material related to this article can be found, in the online version, at https://www.mdpi.com/article/10.3390/catal11040516/s1, Figure S1: XRD patterns of ZnO/PAA2 using different washing, Figure S2: TGA curves of ZnO/PAA2 using different washing, Figure S3: XRD diffraction patterns for ZnO/PAA5 washed with different volume of EtOH, Figure S4: TGA curves for ZnO/PAA5 washed with different volume of EtOH, Figure S5: TGA curves for ZnO/PAA2 synthesized at different temperature, Figure S6: TGA cuves of ZnO/PAA5 synthesized at different temperature, Figure S7: TGA curves for ZnO/PAA2 calcined at different temperatures, Figure S8: TGA curves for ZnO/PAA5 calcined at different temperatures, Figure S9: (a) XRD diffraction pattern and (b) TEM images of commercial ZnO, Figure S10: Representative XRD diffraction patterns of 5%Cu/ZnO_{20} at different stage of the synthesis, Figure S11: Conversion and selectivity in function of time for Cu supported on commercial ZnO with different copper weight percentage, Figure S12: XRD patterns of 2.5%Cu/ZnO_{20} and 20%Cu/ZnO_{20} before and after reaction, Figure S13: XRD patterns of 10%Cu/ZnO_{20} and 10%Cu/ZnO_{80} before and after reaction, Figure S14: TEM images of 10%Cu/ZnO_{20} (a, c) and 10%Cu/ZnO_{80} (b, d) before (a, b) and after (b, d) reaction, Figure S15: Selectivity towards 1,2-propanediol in function of conversion, Figure S16: XRD patterns of the fresh 20%Cu/ZnO-$PAA2_{0\text{-}NC}$, after 6h and 24 h of reaction, Figure S17: XRD patterns of the fresh and reused catalysts (20%Cu/ZnO-$PAA2_{0\text{-}NC}$). Table S1: Cu/Zn molar ratios, amount of 1,2

PDO produced per mol of Cu and initial rates (V_0) associated with Cu supported on commercial ZnO. Table S2: Cu/Zn molar ratios and amount of 1,2 PDO produced per mol of Cu associated with Cu/ZnO/PAAX.

Author Contributions: Conceptualization, N.P. and S.D.; methodology, N.P. and S.D.; validation, N.P. and S.D.; formal analysis, L.O.; investigation, L.O.; resources, N.P. and S.D.; writing-original draft preparation, L.O.; writing-review and editing, N.P. and S.D.; supervision, N.P. and S.D.; project administration, N.P. and S.D.; funding acquisition, L.O., N.P. and S.D. All authors have read and agreed to the published version of the manuscript.

Funding: This research received no external funding and APC was funded by IRCELYON.

Acknowledgments: L.O. acknowledges the Lebanese association Daw for the financial support. The authors thank in particular Thibaut CORNIER and the members of the IRCELYON scientific platforms for their assistance in the characterization of catalysts.

Conflicts of Interest: The authors reported no declarations of interest.

References

1. Monteiro, M.R.; Kugelmeier, C.L.; Pinheiro, R.S.; Batalha, M.O.; da Silva César, A. Glycerol from biodiesel production: Technological paths for sustainability. *Renew. Sustain. Energy Rev.* **2018**, *88*, 109–122. [CrossRef]
2. Mota, C.; Peres Pinto, B.; de Lima, A.L.A. *Glycerol, A Versatile Renewable Feedstock for the Chemical Industry*; Springer International Publishing: Cham, Switzerland, 2017; ISBN 978-3-319-59374-6.
3. Pagliaro, M.; Ciriminna, R.; Kimura, H.; Rossi, M.; Della Pina, C. From glycerol to value-added products. *Angew. Chem. Int. Ed.* **2007**, *46*, 4434–4440. [CrossRef] [PubMed]
4. Samudrala, S.P. Glycerol transformation to value-added 1,3-propanediol production: A paradigm for a sustainable biorefinery process. In *Glycerine Production and Transformation, an Innovative Platform for Sustainable Biorefinery and Energy*; Frediani, M., Ed.; IntechOpen: London, UK, 2019.
5. EFSA. Panel on Food Additives and Nutrient Sources added to Food (ANS). *EFSA J.* **2018**, *16*, s1006.
6. Auneau, F.; Michel, C.; Delbecq, F.; Pinel, C.; Sautet, P. Unravelling the mechanism of glycerol hydrogenolysis over rhodium catalyst through combined experimental–theoretical investigations. *Chem. Eur. J.* **2011**, *17*, 14288–14299. [CrossRef] [PubMed]
7. Vasiliadou, E.; Heracleous, E.; Vasalos, I.; Lemonidou, A. Ru-based catalysts for glycerol hydrogenolysis—Effect of support and metal precursor. *Appl. Catal. B Environ.* **2009**, *92*, 90–99. [CrossRef]
8. Dasari, M.A.; Kiatsimkul, P.-P.; Sutterlin, W.R.; Suppes, G.J. Low-pressure hydrogenolysis of glycerol to propylene glycol. *Appl. Catal. A Gen.* **2005**, *281*, 225–231. [CrossRef]
9. Montassier, C.; Giraud, D.; Barbier, J.; Boitiaux, J.P. Polyol transformation by liquid-phase heterogeneous catalysis over metals. *Bull. Soc. Chim. Fr.* **1989**, *2*, 148–155.
10. Mai, C.T.Q.; Ng, F.T.T.; Rempel, G.L. Recent advances on the conversion of glycerol to acrolein, 1,3-propanediol, propanol and propylene using acidic heterogeneous catalysts. *Catalysis* **2018**, *30*, 176–222.
11. Chaminand, J.; Djakovitch, L.; Gallezot, P.; Marion, P.; Pinel, C. Glycerol hydrogenolysis on heterogeneous catalysts. *Green Chem.* **2004**, *6*, 359–361. [CrossRef]
12. Wang, S.; Liu, H. Selective hydrogenolysis of glycerol to propylene glycol on Cu–ZnO catalysts. *Catal. Lett.* **2007**, *117*, 62–67. [CrossRef]
13. Balaraju, M.; Rekha, V.; Prasad, P.S.S.; Prasad, R.B.N.; Lingaiah, N. Selective Hydrogenolysis of Glycerol to 1, 2 Propanediol over Cu–ZnO Catalysts. *Catal. Lett.* **2008**, *126*, 119–124. [CrossRef]
14. Bienholz, A.; Schwab, F.; Claus, P. Hydrogenolysis of glycerol over a highly active CuO/ZnO catalyst prepared by an oxalate gel method: Influence of solvent and reaction temperature on catalyst deactivation. *Green Chem.* **2010**, *12*, 290–295. [CrossRef]
15. Wang, S.; Zhang, Y.; Liu, H. Selective hydrogenolysis of glycerol to propylene glycol on cu-zno composite catalysts: Structural requirements and reaction mechanism. *Chem. Asian J.* **2010**, *5*, 1100–1111. [CrossRef]
16. Yue, C.-J.; Zhang, Q.-Y.; Gu, L.-P.; Su, Y.; Zhu, S.-P. Hydrodynamics of binary mixtures in a tapered gas–solid fluidized bed. *Asia Pac. J. Chem. Eng.* **2014**, *9*, 581–590.
17. Gao, Q.; Xu, B.; Tong, Q.; Fan, Y. Selective hydrogenolysis of raw glycerol to 1,2-propanediol over Cu–ZnO catalysts in fixed-bed reactor. *Biosci. Biotechnol. Biochem.* **2016**, *80*, 215–220. [CrossRef]
18. Durán-Martín, D.; Granados, M.L.; Fierro, J.L.G.; Pinel, C.; Mariscal, R. Deactivation of CuZn catalysts used in glycerol hydrogenolysis to obtain 1,2-propanediol. *Top. Catal.* **2017**, *60*, 1062–1071. [CrossRef]
19. Pandey, D.K.; Biswas, P. Production of propylene glycol (1,2-propanediol) by the hydrogenolysis of glycerol in a fixed-bed downflow tubular reactor over a highly effective Cu–Zn bifunctional catalyst: Effect of an acidic/basic support. *New J. Chem.* **2019**, *43*, 10073–10086. [CrossRef]
20. Wang, C.; Jiang, H.; Chen, C.; Chen, R.; Xing, W. Solvent effect on hydrogenolysis of glycerol to 1,2-propanediol over Cu–ZnO catalyst. *Chem. Eng. J.* **2015**, *264*, 344–350. [CrossRef]

21. Du, Y.; Wang, C.; Jiang, H.; Chen, C.; Chen, R. Insights into deactivation mechanism of Cu–ZnO catalyst in hydrogenolysis of glycerol to 1,2-propanediol. *J. Ind. Eng. Chem.* **2016**, *35*, 262–267. [CrossRef]
22. Hou, M.; Jiang, H.; Liu, Y.; Chen, R. Role of initial water content in glycerol hydrogenolysis to 1,2-propanediol over Cu–ZnO catalyst. *React. Kinet. Mech. Catal.* **2017**, *122*, 1129–1143. [CrossRef]
23. Daniele, S.; Cornier, T.; Valette, A. Composition Aqueuse de Particules de ZnO Suspendues. Patent FR20141458575, 3 April 2021.
24. Zhu, Y.; Apostoluk, A.; Gautier, P.; Valette, A.; Omar, L.; Cornier, T.; Bluet, J.M.; Masenelli-Varlot, K.; Daniele, S.; Masenelli, B. Intense visible emission from ZnO/PAAX (X = H or Na) nanocomposite synthesized via a simple and scalable sol-gel method. *Sci. Rep.* **2016**, *6*, 23557. [CrossRef]
25. Zhang, Y.; Apostoluk, A.; Theron, C.; Cornier, T.; Canut, B.; Daniele, S.; Masenelli, B. Doping of ZnO inorganic-organic nanohybrids with metal elements. *Sci. Rep.* **2019**, *9*, 1–10. [CrossRef] [PubMed]
26. Nicholas, N. Control of ZnO Crystal Morphology through Face Specific Absorption. Ph.D. Thesis, University of Melbourne, Melbourne, Australia, 2011.
27. Delannoy, L.; Thrimurthulu, G.; Reddy, P.S.; Méthivier, C.; Nelayah, J.; Reddy, B.M.; Ricolleau, C.; Louis, C. Selective hydrogenation of butadiene over TiO_2 supported copper, gold and gold–copper catalysts prepared by deposition–precipitation. *Phys. Chem. Chem. Phys.* **2014**, *16*, 26514–26527. [CrossRef]
28. Karelovic, A.; Ruiz, P. The role of copper particle size in low pressure methanol synthesis via CO_2 hydrogenation over Cu/ZnO catalysts. *Catal. Sci. Technol.* **2015**, *5*, 869–881. [CrossRef]
29. Van den Berg, R. Formation, Activity and Growth of Copper Nanoparticles in Methanol Synthesis Catalysts. Ph.D. Thesis, University of Utrecht, Utrecht, The Netherlands, 2016.
30. Mizugaki, T.; Arundhathi, R.; Mitsudome, T.; Jitsukawa, K.; Kaneda, K. Selective hydrogenolysis of glycerol to 1,2-propanediol using heterogeneous copper nanoparticle catalyst derived from Cu–Al hydrotalcite. *Chem. Lett.* **2013**, *42*, 729–731. [CrossRef]